Materials Advances

ROYAL SOCIETY OF CHEMISTRY

PAPER

View Article Online
View Journal | View Issue

Cite this: *Mater. Adv.*, 2025, **6**, 1914

Hierarchical intrafibrillar mineralization with EGaIn nanocapsules through a one-step collagen self-assembly approach†

Kevin H. Mwangi, [a] Yue Qu, [b] Sengpav Tong, [a] Xiaodan Sun, [a] Lingyun Zhao [a] and XiuMei Wang *[a]

Received 2nd December 2024,
Accepted 3rd February 2025

DOI: 10.1039/d4ma01186d

rsc.li/materials-advances

Inspired by nature, various engineered mineralized collagen composites have been successfully synthesized through biomimetic processes, providing insights into the underlying mechanisms of natural biomineralization. Due to its low toxicity, EGaIn liquid metal has garnered attention in a wide range of emerging areas and is increasingly being studied at the frontiers. Collagen fibrils serve as templates for the creation of modern models of intrafibrillar biomineralization mechanisms. In order to create a potent osteoinductive biomimetic, this study looked at the collagen-EGaIn matrix adoption in intrafibrillar biomineralization of collagen matrix constructs. To the best of our knowledge, it is the first time that intrafibrillar mineralization of PEG-EGaIn-Col-Ap matrices was achieved *via* a one-step approach, where collagen fibrils served as a templating matrix, and as a surfactant. The result showed that PEG-EGaIn nanocapsules with collagen microfibrils formed an efficient matrix for the growth of acicular apatite. Electron microscopy and characterization analyses revealed that the presence of ethanol significantly enhanced the infiltration of mineral nucleation precursors into the interior spaces of collagen fibrils, which facilitated hierarchical intrafibrillar mineralization. The integration of novel materials holds promise for enhancing the osteogenic properties of these biomaterials, ultimately contributing to improved orthopedic treatments.

Introduction

Natural bone and dentin tissues derive their exceptional biomechanical attributes from the exquisite co-assembly of collagen fibers and apatite nanocrystals. Inspired by this intrinsic microstructure, researchers have embarked on the creation of advanced mineralized collagen nanocomposites with diverse biomimetic mineralization properties (readers are encouraged to read any of these reviews).[1–6] This paradigm shift not only elucidates the subtle details of natural biomineralization but also paves the way for the development of novel nanocomposite biomaterials with enhanced functionalities.[7]

A critical challenge in replicating the intricate patterns of mineral deposition within collagen fibrils remains a topic of ongoing debate, despite significant advancements. Polymer additives, such as anionic and cationic polyelectrolytes, act akin to non-collagenous proteins (NCPs) in stabilizing mineral nucleation—a critical step for intrafibrillar and interfibrillar mineralization mirroring the nanoarchitecture of bone.[8] Techniques like the polymer-induced liquid precursor (PILP) method employ polyelectrolytes, such as PAA, PAsp, and PVPA, to replicate the role of NCPs in promoting or inhibiting mineral nucleation, growth, and crystallization, directing the precise location of mineral deposits within collagen's nanostructure. Recent studies have underscored the significance of prenucleation cluster stabilization in the biomineralization process of collagen-templated calcium phosphate (CaP). These clusters are crucial intermediates that influence the effective onset of mineralization within collagen fibrils. The presence of nucleation stabilizers, such as NCPs, ensures the orderly alignment of mineral platelets at the nanoscale, reflecting natural bone's complex arrangement.[9–12]

Recent studies have indicated that ultrafine collagen fibers intended for biological applications have involved the use of ethanol systems as co-solvents.[13,14] It has been reported that collagen remains soluble at ethanol concentrations below 50%, regardless of the method of ethanol addition. The triple helix of collagen exhibits kinetic stability in the presence of low ethanol concentrations ($\leq$40%, v/v) at low temperatures, but it becomes thermodynamically unstable as the concentration of ethanol increases.[14] Notably, Jee *et al.* investigated the

[a] State Key Laboratory of New Ceramics and Fine Processing, Key Laboratory of Advanced Materials, School of Materials Science and Engineering, Tsinghua University, Beijing 100084, China. E-mail: wxm@mail.tsinghua.edu.cn
[b] Department of Medicine, School of Life Science, Center of Biology, Tsinghua University, Beijing 100084, China

† Electronic supplementary information (ESI) available. See DOI: https://doi.org/10.1039/d4ma01186d

infiltration of ethanol into demineralized dentin collagen fibrils, employing molecular dynamics (MD) simulations to elucidate the interactions between ethanol, bound water, and collagen structures[15] unveiling unique insights into the interplay between ethanol, bound water, and collagen structures. The researchers identified three distinct hydration layers surrounding the collagen molecules, with two inner layers (0.15–0.43 nm) hosting tightly bound water, essential for collagen's structural integrity, and an outer layer (0.43–0.63 nm) occupied by loosely bound water. Strikingly, ethanol was shown to significantly reduce roughly 50% of the loosely bound water in the third layer without affecting the tightly bound water in the inner layers. This result is in accordance with the report by Chiba *et al.* where the study challenges earlier assertions that collagen molecules in dentin are too densely packed to permit monomer infiltration, instead suggesting that the presence of tightly bound water does not hinder the diffusion of adhesive resin monomers. The authors propose that the removal of unbound water through ethanol treatment enhances the potential for effective resin infiltration, which is crucial for the durability of resin–dentin bonds.[16] However, these studies have limitations, primarily the exclusion of non-collagenous proteins that may influence the collagen matrix's structural properties and its interaction with solvents. As a result, further exploration of these concepts in clinical contexts could unlock new strategies for improving patient outcomes especially in dentin and bone restoration.

Liquid metal (LM) alloys based on gallium, notably EGaIn and Galinstan, are receiving increased attention for their unique properties, including low toxicity, adaptability, conductivity, and high radiographic density, positioning them as valuable assets for various biomedical applications.[17,18] In particular, bestowed by their unique low cytotoxicity, biocompatibility, morphologic transformability and high radiographic densities, Ga-alloys offer a plethora of applications especially in biomedical expansion such as in drug delivery systems, nerve connection, tumour therapy, and molecular imaging.[19–22] Despite the prevailing view of EGaIn's low toxicity, there have been limited investigations into the potential toxicity of this nanomaterial.[18,21] Hence, questions remain about the cytotoxicity and biocompatibility of gallium and indium ions, influenced by variables such as the cell type, exposure duration, and ion concentration. Surface modification techniques are integral to the production of stable EGaIn nanocapsules, utilizing agents like thiol, catechol, phosphonic acid, trithiocarbonate, carboxylic acid, amine and polyethylene glycol.[17,23,24] Nevertheless, certain approaches for altering the surface of the liquid-phase alloy mentioned above are not only unfeasible but also intricate, making them less applicable (bench to bedside). As a result, a straightforward technique for producing stable and easily manageable liquid-phase alloy particles that can endure physiological conditions and hinder the unwanted formation of oxide nanorods. The elemental LM nanomaterial could be extremely advantageous in the field of biomedical applications, such as sensing, imaging, and disease treatment.

Intrinsically, mineralized collagen fibrils display remarkable biomechanics and biocompatibility but lack adequate osteoinductive capacity, hindering their utility in bone repair.[25–28] Enhancing the osteogenic properties of these fibrils is imperative for optimizing their application in orthopedic treatments.

An alternative strategy to accomplish dopant-induced osteogenesis is to include an inorganic component in the material. For example, attempts have been made by modifying the mineral apatite with carbon dots, silver (Ag), gold (Au), zinc (Zn) or iron (Fe) to enhance bone regeneration.[28–31] The study proposes a "nano-matrix interface" combining a novel metal (liquid metal in this case) with an established biomimetic mineralization strategy, focusing on hierarchical intrafibrillar mineralization within a benign collagen–ethanol system. The hypothesis postulates that the combination of PEG-EGaIn with collagen fibrils under controlled ethanol concentrations should not compromise mineral nucleation stability, thus improving the mineralization arrangement within collagen.

This integrative approach, centered around the dual functionality of bionics, explores the synergistic effects of novel metals and biomimetic strategies on osteogenic enhancement. Mineralized collagen fibrils prepared using a 20% ethanol concentration in the mineralization system exemplify the development of dopant-induced smart tissue engineering biomimetics. These advancements represent a stepping stone in the evolution of biomaterials for bone repair and regeneration, underscoring the potential for innovative solutions in orthopedic treatments and tissue engineering.

Results

Initial amorphous nucleation and crystallization stage of biomimetic mineralization

Type I collagen exhibited good solubility in acidic solutions, forming a transparent and stable aqueous solution. Upon the addition of aqueous benign-ethanol, there were no significant changes in the solution's appearance, nor was there any flocculation or precipitation, indicating that ethanol did not denature the collagen molecules. After the addition of Ca^{2+} and PAA/PO_4^{3-}, the aqueous solution in both mineralization systems become translucent gradually from the initial transparent appearance, accompanied by the formation of the prenucleation clusters and then agglomerate and nucleate into ACP precursors. At the early stage of mineralization within 12 h after neutralization, both of the mineralization systems kept a homogenous emulsion-like appearance without obviously detectable precipitations, indicating the stabilized nucleation regulated by the organic templates of collagen and HPAA. The *in situ* co-assemblies of ACP minerals and collagen fibrils were visualized by TEM, as shown in Fig. 1. Remarkable differences on the mineralized collagen fibrils prepared in the aqueous collagen systems with or without ethanol respectively were observed. First, it is worth noting that the collagen fibrils assembled in the ethanolic-HPAA mimetic (ethanolic-Col-Ap) were much thicker than those in the water-mediated HPAA

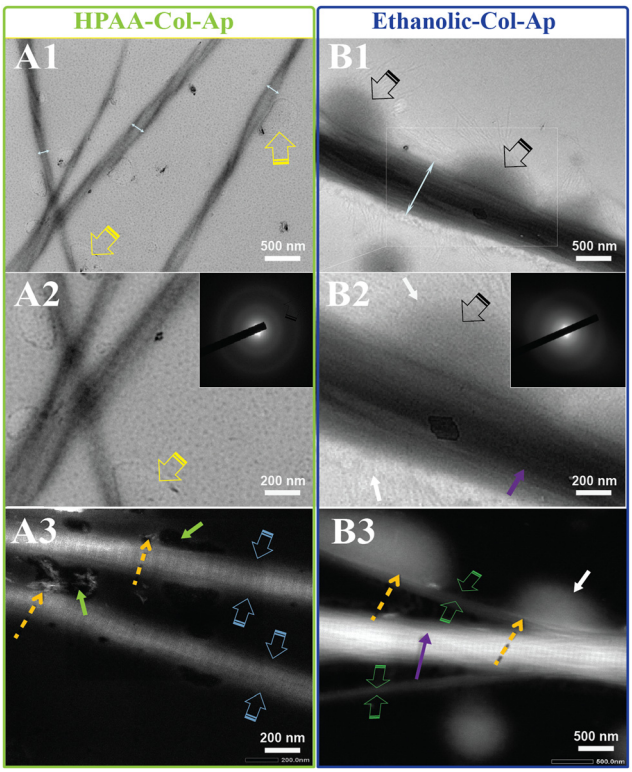

Fig. 1 Characterization of the early biomineralization phase between HPAA Col-Ap and the ethanolic Col-Ap constructs. (A1)–(A3) The high magnification TEM tomograph of the HPAA Col-Ap mimetics reveals significant agglomeration, which leads to the loss of the transient metastable CaP solution globule initial transparency upon consolidation (yellow open arrows). (A2) An enlarged view of the marked region on the right side of the control specimen shows numerous nanograins (presumably CaP precursors) dispersed within the matrix. SAED from isolated fluidic goblet in [(A2)] reveals the amorphous phase (B1)–(B3) TEM tomograph of the ethanolic Col-AP mimetic depicting the initial stage of ACP precursors interacted with collagen fibrils in the presence of benign aqueous ethanol and HPAA as a regulator (B1) and (B2) high magnification EM tomograph of the ethanolic Col-AP mimetic showcases fluidic amorphous globules (denoted by black open arrows). SAED from isolated fluidic goblet in [(B2)] reveals the amorphous phase. Remarkably, in both lamellar mimetics, the interface is clearly identifiable, with no detectable crevices, indicating excellent interfacial bonding between both collagen lamellar matrices. (A3) Representative HAADF-STEM images of HPAA Col-Ap mimetic where ACP precursors (green arrows) collagen fibrils (pale blue open arrows), precursor nucleation (orange dashed arrows) (B3) HAADF-STEM image of ethanolic Col-Ap mimetic displays a clear distinct portion between infiltration of intrafibrillar mineral (marked by purple arrows) and unimpregnated fibril (marked by green open arrows) within the braided collagen microfibril. A distinct region of the collagen fibril is partly entrenched with intrafibrillar minerals and amorphous ACP precursors (marked by orange dashed arrows).

mimetic (HPAA Col-Ap), with the diameters in the range of 300–500 nm and 50–200 nm, respectively.

The enhanced self-association of collagen with ethanol involvement is probably a result of the dehydrating effect of ethanol, which removes the loosely bound water surrounding collagen molecules, thus decreasing the water-mediated hydrogen bonds and increasing the inter-molecular interactions *via* hydrophobic and electrostatic forces. During the biomimetic mineralization process, the collagen templates are firstly incubated with calcium ions for at least 12 hours and then PAA/phosphate solution is added dropwise for nucleation. Therefore, the calcium/phosphate ions and preformed PAA-stabilized ACP precursors infiltrate into the interconnecting water-filled intrafibrillar spaces of collagen fibrils including the gap zones, which is accelerated by the dehydration effect of ethanol. Moreover, distinct cross-banding pattern became discernible within the dark-field EM and the collagen fibril showcased bright streaks suggestive of metastable prenucleation phase within the nanodomains of the collagen molecules (Fig. 1B3). In contrast, no obvious intrafibrillar mineralization (low contrast image in regular bright-field mode, Fig. 1A1) was visualized in the HPAA Col-Ap matrices because of the extended nucleation stage. Furthermore, collagen fibrils in both systems exhibited a typical uniform 67-nm periodicity in Fig. 1A3 and B3 (as denoted by pale blue and green open arrows, respectively), implying that the addition of ethanol did not denature collagen molecules and disrupt their self-assembly. Noticeably, it can be observed in Fig. 1B1 and B2 that amorphous globules with diameters ranging from 50 to 300 nm are homogeneously and spatially distributed along the mineralized collagen fibrils, which may lead to intra- and interfibrillar mineralization.

It is interesting that many transparent radial filaments sprouted from these globular droplets and collagen fibrils outward, suggestive of percolation (denoted by pale blue open arrow). Nevertheless, there was no discernible phase separation and precipitation in the ethanolic Col-Ap matrices. Noticeably, similar PILP globular structures could be seen, adsorbed to the braided HPAA Col-Ap matrices (Fig. 1A1 and A2, denoted by yellow open arrows and green arrows). The amorphous particle diameter is in perfect agreement with those determined using TEM. A possible explanation for this is the reduced concentration of ionic precursors, likely due to the water present within the droplet. Conversely, the amorphous globules in the ethanolic Col-Ap matrices (Fig. 1B1 and B2, denoted by black open arrows) transitioned from transparent to translucent "darker appearance", indicating a potential degree of agglomeration of the ionic precursors likely induced by the gradual removal of water by ethanol. Additionally, dark-field view (Fig. 1A3 and B3), for the HPAA Col-Ap and ethanolic Col-Ap matrices correlated the amorphous globules (denoted by orange dashed arrows) being fluidic in nature (denoted by green arrows and white arrows respectively).

After three days of mineralization, small deposits of apatite crystals formed in a disordered manner on the surface of the HPAA Col-Ap mimetic, as shown in Fig. 2A (middle and left; marked by pointers), indicating a random orientation of the crystallites' *c*-axis (see inset, SAED). In contrast, the ethanolic Col-Ap mimetic surface did not exhibit surface mineralization. However, the oriented *c*-axis of the acicular mineral (see inset, SAED) was confined within the interstitial spaces of the continuous braided-collagen fibrils, which is illustrated by the dark contrast in Fig. 2A2 (middle right; marked by pointers). Although at low contrast, discrete unmineralized segments (mid-phase) were observed within the heavily mineralized fibrils (Fig. 2, marked by yellow open arrows) in both mimetics.

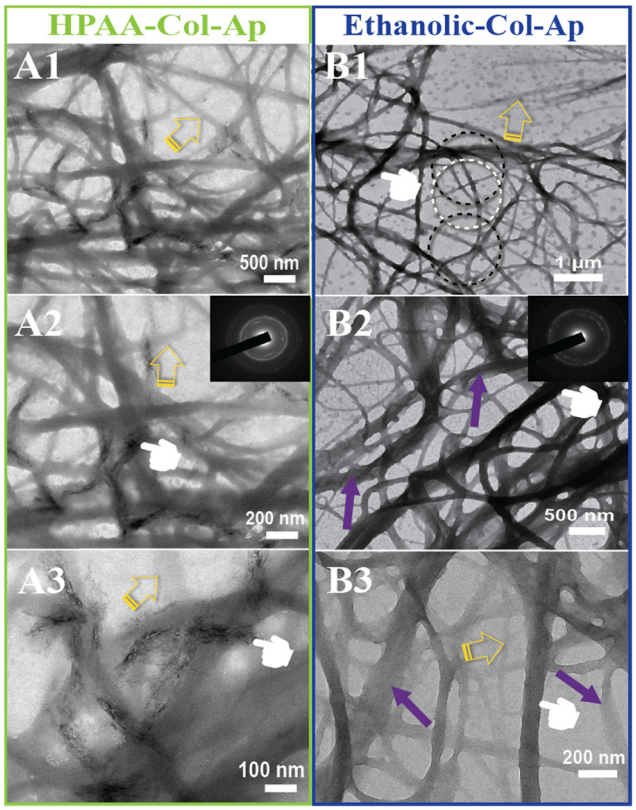

Fig. 2 Unstained conventional TEM of intra-interfibrillar mineralization on HPAA Col-Ap and ethanolic Col-Ap mimetics (A) and (B). (A1)–(A3) EM tomography displays hierarchical bundled-like arrangements of HPAA Col-AP mimetic following 72 h incubation. In the HPAA Col-Ap mimetic, interfibrillar mineralization with discrete electron-dense strand of individual microfibrils were observed (pointers) on the surfaces of the collagen membranes. Scale bars: 500 nm (left), 200 nm (middle left) and 100 nm (bottom left). (B1)–(B3) EM tomography of the ethanolic Col-Ap mimetic showcasing hierarchical intrafibrillar bundled-like arrangements of mineralized collagen following 72 h incubation (pointers). A representative example (B1) depicting distinct regions of partially mineralised portions (indicated by white dotted circles) were observed within the well-organized and highly filled intrafibrillar minerals (denoted by black dotted circles) of the same fibril. Notably, it is possible to discern that the collagen fibril was already entrenched with intrafibrillar minerals (probably represent the irregular profiles of the intrafibrillar ACP) (purple arrows). At low contrast, the silhouettes of continuously braided microfibrils could be vaguely discerned. These unmineralized regions had not been infiltrated by the prenucleated ACP droplets, which were denoted by the yellow open arrows (see also [(A1–A3)]). Scale bars: 1 μm (right), 500 nm (middle left) and 200 nm (bottom right).

Additionally, the diameter of the continuous braided ethanolic Col-Ap mimetic increased (Fig. 2B2 and B3; marked by purple arrows) in comparison to that of the partially or unmineralized segments (Fig. 2B1–B3; marked by yellow open arrows). This event occurs temporarily during the early intrafibrillar mineralization of collagen fibrils as the fibril becomes fully infiltrated (denoted by purple arrow) with the amorphous fluid-like ACP precursors as it transitions into more crystalline phase within the confinement of the collagen interstitial spaces.

Interestingly, the fluidic-like amorphous ACP and acicular minerals were observed exclusively in well-organized regions of the collagen fibril, as illustrated in Fig. 2B1–B3 (right) and Fig. S2B1, B2 (ESI†) (marked by black dotted circles). Conversely, segments characterized by poor organization exhibited minimal intrafibrillar mineralization, predominantly consisting of a few randomly oriented acicular minerals, as shown in the same segment (marked by white dotted circles). These observations suggest that the aqueous benign ethanol system not only facilitates the infiltration of acicular minerals but also directs the orientation and growth of acicular apatite. Furthermore, as intrafibrillar mineralization progresses and becomes oriented, the collagen fibrils expand parallel to their longitudinal axis, undergoing deformation due to the transition mineral as evidenced by discrete striated textures, as indicated in Fig. 2B2, B3 and Fig. S2B1, B2 (ESI†) (marked by black dotted circles). However, this is in stark contrast to the HPAA Col-Ap mimetic at 24–48 h as indicated in Fig. S1 and S2A1, A2 (ESI†).

Apatite phase transformation and propagation during interfibrillar mineralization in the HPAA Col-Ap mimetic

The element mapping examination (EDX) indicates the integration of the apatite mineral phase along the braided collagen fibril and their relatively uniform structure. The element mapping from the HPAA Col-Ap mimetic suggests that the matrices was much more mineralized at the end of mineralization period at day 7 (Fig. 3A). Moreover, under EM observation at day 4–5, the high-contrast region (Fig. 3B; marked by white arrows) is defined as the interfibrillar mineralization structure, revealing discrete acicular apatite that were more heavily stacked along the fibril revealing faint cross-banding patterns of intrafibrillar mineralization (Fig. 3B; marked by white arrows). Elemental mapping using (Fig. 3A) revealed that the degree of interfibrillar mineralisation of the collagen fibril comprised of elemental calcium (Ca) and phosphate (P) crystals (Ca/P) (Fig. 3B inset from A) with an atomic ratio of 1.55 ± 0.12 that has a close elemental stoichiometry to that of natural bone of 1.67.

The electron diffraction (SAED) of those fibrils resulted in arc-shaped patterns along the (002) diffraction plane that followed the co-alignment of the highly hierarchical *c*-axes of the acicular nanoplatelets and grew in an orderly manner along the longitudinal axis of the mineralized fibril (Fig. 3B, marked by the green arrow). After 7 days of mineralization, the HPAA Col-Ap mimetic was completely covered by disorderly acicular nanocrystals (Fig. 3C).

Apatite phase transformation and propagation during intrafibrillar mineralization in the ethanolic Col-Ap mimetic

To demonstrate intrafibrillar mineralization, the ethanolic Col-Ap mimetic were loaded onto EM grids and analyzed. Under EM observation, the fibers expand laterally as a result of water dehydration and absorption due to fluctuations in both pH and amorphous ACP precursors (Fig. 4A; see also Fig. 2B1 and B2 and Fig. S1A (ESI†) marked by purple arrows) prompting swollen fibrils (measured *ca.* 300–500 nm) perturbation in the lateral dimensions.[32] As the transformation from amorphous ACP into mineral apatite takes place temporarily during the initial mineralization stages (mid-phase to late-phase), the

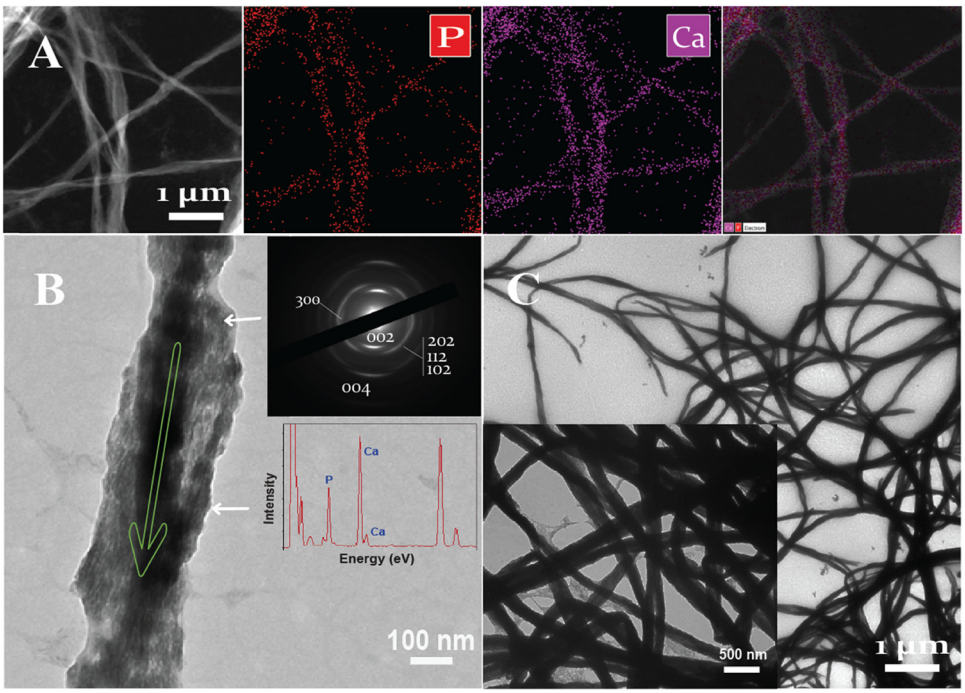

Fig. 3 Unstained conventional TEM interfibrillar mineralization of the HPAA Col-Ap mimetic mid- and late phase. (A) EM tomography of HPAA Col-Ap mimetic depicting element mapping in the TEM model for the mineralized collagen matrices further confirming the hierarchical intra-interfibrillar apatite assembly within the continuously braided microfibrils. Scale bar: 1 µm. (B) The *c*-axis of all acicular nanocrystals (*ca.* 10 nm × 20 nm) was oriented parallel to the longitudinal axis of the collagen fibers (green arrow), resulting in the crystals growing in a structured and orderly manner along the fibers' length. Collagen banding was vaguely recognized because there was heavy mineralization along the rest of the fibril (white arrows) of the supporting carbon film. However, defect within the fibrils reveals individual intrafibrillar mineral crystallites. Selected area electron diffraction of the fibril shown in (B), (left) (see inset) confirmed that the mineral phase is apatite. The (002) diffraction plane is arc-shaped and is oriented parallel to the longitudinal axis of the mineralized fibril (green arrow). The spectra concentration (TEM-EDX, from (A)) matched to those of mineral crystallites with a Ca/P ratio of 1.67. Scale bar: 100 nm. (C). Representative EM micrograph of the nearly completed interfibrillar mineralization of the HPAA ColHA lamellar mimetic following the end of the mineralization period. Scale bar: 1 µm.

intrafibrillar water compartments of the collagen fibril is gradually eliminated due to the presence of benign-aqueous ethanol[15] while the amorphous ACP droplets are being deposited within the fibrillar milieu (dashed circles: Fig. 4B). In the early phase of mineralization (24–48 h), the collagen fibers undergoes a transient enlargement in their lateral spacings, which is likely due to the infiltration of amorphous CaP precursors *via* the PILP mechanism,[33,34] which is in stark contrast to the HPAA Col-Ap mimetic (Fig. S1 and S2A1, A2, ESI†). In this case, residual PILP globules can be observed adhered to the woven collagen fibrils. The benign-aqueous ethanol likely removes water molecules from within the collagen fibril, causing rearrangement of intermolecular bonds and closer packing of collagen molecules. When it comes to the mechanism of ethanol interaction, it was illuminated that the ethanol molecules bind to the water-mediated hydrogen-bond rather than collagen triple helix, causing distortion and rearrangement of intra- and intermolecular bonds possibly due to its dehydrating effect.[15,35] Moreover, the density content of compositional water in the inter-cluster gaps became more readily available stemming from the molecular displacement, corresponding to the lateral spacings of the collagen fibril[15] and therefore promoting the fluid-like amorphous ACP precursors infiltrating the nanoscopical interstices of the collagen fibrils.[33,34,36] Ethanol treatment appears to inhibit interfibrillar mineralization, possibly leading to a more controlled and confined mineral deposition within the collagen fibrils (Fig. 4B marked by white arrows; Fig. 2B1–B3 and Fig S2B1, B2, ESI†). Moreover, acicular nanoplatelets grew in orderly manner and oriented in a way that their (100) planes are roughly parallel to each other and their crystallographic *c*-axes lie parallel to the collagen membrane long axes. (Fig. 4B, marked by green arrow). The decreased spacing between collagen fibrils following dehydration is caused, at level I, by water molecules that are present between these interstitial spaces of collagen molecules "gate-keeper".[14,15,33,37,38] The transition of these intrafibrillar ACP minerals from the fluidic amorphous state to apatite crystallites along the fibril's *c*-axis,[39] could be demonstrated from the loosely packed, diffuse patterns *via* SAED (Fig. 4C).

Still, progressively noticeable fluidic ACP remnant globules could be identified adjacent to adsorbing within the vicinity of the collagen fibril with concomitant to hierarchical intrafibrillar apatite became heavily stacked along the microfibrillar gap zones of the fibril and this is best appreciated in (Fig. 4D, E; marked by white arrows) as they become denser, resulting in vague cross-banding to distinct cross-banding pattern after 96 h indicative of the *c*-axis hierarchical alignment. In addition, interfibrillar mineralised fibrils were linked by acicular apatite

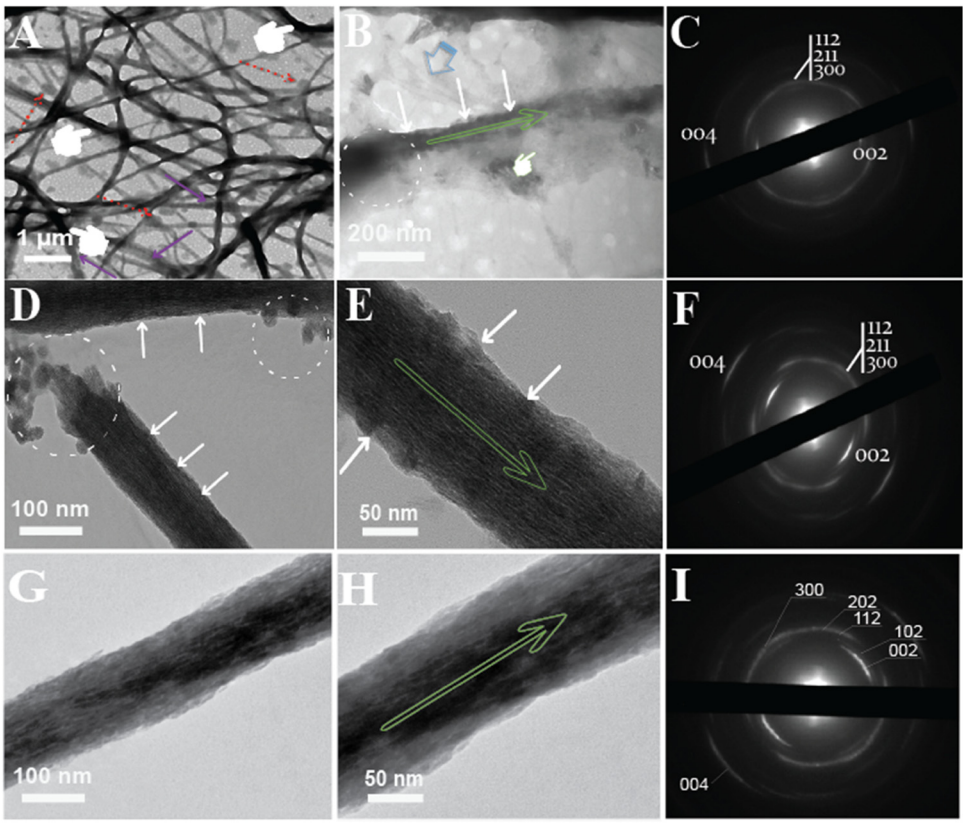

Fig. 4 Unstained conventional TEM of intra-interfibrillar mineralization of the ethanolic Col-Ap mimetic. (A) EM tomography depicting spatiotemporal events at 72 h within the microstructures of the collagen fibers. Remnant PILP droplets can be seen adsorbing to the fibers (denoted by red dashed arrows). The microstructures of the collagen depicted by the (pointer), is already entrenched with intrafibrillar minerals. Scale bars represent 1 μm and 200 nm. (B) High magnification showcases an isolated microfibrils revealing discrete hierarchical assembly of intrafibrillar acicular nanoplatelets stacking along the gap zones revealing periodic cross-banding distribution of the intrafibrillar minerals (white arrows). It is important to note that intrafibrillar mineralization seem to occur even in the presence of aqueous ethanol (pointer). (C) Corresponding SAED pattern from [(B)]. (D) EM tomography of an isolated collagen fibril illustrating a partially mineralized microfibril revealing large remnants of irregular intrafibrillar ACP droplets (dashed circles) seen being deposited within the isolated microfibrillar membrane. Scale bars represent 100 nm. (E) High magnification TEM micrograph from [(D)] reveals a distinct striated texture (denoted by white arrows). Scale bars represent 50 nm. (F) Corresponding SAED patterns from [(E)] reveal distinctive to collagen signature along the 002 and 004 diffraction plane. The apparent continuous ring patterns corresponds to the acicular nanoplatelets with (1122), (211), (300) and (310) diffraction signatures matching those of crystalline apatite. (G) After incubating for over 5 days, heavy interfibrillar deposition interfibrillar mineralization which consisted of an isolated array of mineral strand. Scale bar 100 nm. (H) High magnification TEM, showcases electron-dense with acicular apatite that grew on the surface of the isolated fibril. Scale bar 50 nm. (I) SAED pattern of the fibril taken from [(H)], depicts a clearly crystalline diffraction pattern, indicating interfibrillar arrangement of crystallite nanoplatelets along the long axis of the mineralized part of the collagen fibril (marked by elongated green arrow).

growth on the surface which the apatite *c*-axis lie parallel to collagen membrane long axis (Fig. 4E, marked by green arrow). The orientational axis (demonstrated by 0vc02 and 0vc04 Debye arcs) of the mineralised fibril highlights ordered alignments of the crystals along the *c*-axis and this is depicted *via* SAED pattern. A continuous ring diffraction pattern resembling *in vivo* apatite crystallites had reflections of (112), (211), (300) and (310) (Fig. 4F). In the process of intrafibrillar mineralization, collagen strands are extensively aligned in the axial orientation, but relatively unstructured in the lateral orientation.[40] Thus, the gradual process of dehydration may cause the collagen microfibrils to return to their initial dimensions (non-swollen fibrils (*ca.* 50–200 nm in diameter) once mineralization has been completed (Fig. 4E)).

However, at day 6–7, intrafibrillar mineralization of ethanolic Col-AP mimetic was acquired from a single-isolated collagen fibril model (mature-phase), and this is best illustrated in (Fig. 4G and H) with much coarser apatite crystallites coaligned longitudinally to the surface of the intrafibrillar mineral (Fig. 4H, marked by green arrow). The mineralized ethanolic Col-Ap fibrils demonstrated distinct derby arc patterns with their [0vc02] and [0vc04] planes obtained from electron diffraction (SAED) perpendicular to the fibril's longitudinal axis (Fig. 4I, right), corresponding to the *d*-spacing of collagen fibrils.

Tilting particular sections around the fibril axial direction methodically allowed us to successfully identify these and intermediate patterns (Fig. 4). The electron diffraction patterns in the diffraction area selected for analysis were influenced by all of the crystals. As a result, the crystal's azimuthal orientation or rotation around the *c* axes is quite homogeneous, as can be seen from the distinct differences in the diffraction patterns.

Based on the current study of the ethanolic Col-Ap mimetic, the onset of intrafibrillar mineralization ensemble was easily discernible at day 1 (early stage) as the transient fluidic-like amorphous ACP globules (Fig. 5A, left) transitioned into a crystalline-phase to completely electron-dense braided interfibrillar mineralized collagen fibrils (late-phase) at day 7 (Fig. 5B middle and C, right).

Characterization of microstructures

The different Col-Ap matrices showcased a uniquely hierarchical lamellar microstructure level across the entire cross-section (Fig. 6). On a micro-level, the architecture comprises intricately stacked macro-laminae extending through both Col-Ap matrices (Fig. 6A1 and B1).

This biomimetic characteristic denotes the scaffold potential to facilitate intricate biological interactions, including cell adhesion, proliferation, and differentiation. By integrating macroscopic porosity with micro- and sub micro-level detail, these scaffolds provide an optimized milieu for cellular engagement and bone regeneration, closely emulating physiological conditions.

The kinetics of the different systems on mineralization processes

To better understand the hierarchical arrangement of discrete acicular apatite proposed strategy in this study, the spectroscopical kinetics from retrieved specimens at day 7 for HPAA Col-Ap and ethanolic Col-Ap lamellar matrices were examined under attenuated total reflection–Fourier transform infrared (ATR-FTIR) spectroscopy (Fig. 7A). The crystallization kinetics were characterized by FTIR spectra through the detection of a gradual splitting of the single absorption peaks at 560 and 602 cm^{-1} represent the bending vibrations of ν_4 PO_4 and ν_2 PO_4 respectively. The absorption peaks at 960 and 1020 cm^{-1} were identified as the stretching vibration of ν_1 PO_4^{3-} and ν_3 PO_4^{3-} of the acicular apatite. The absorption peaks at 873 cm^{-1} represent the bending vibration of the ν_2 C–O stretching mode of the carbonate group in the apatite lattice. The bending vibration of ν_3 C–O represents the absorption peaks at 1398 cm^{-1} was also indicative of the presence of acicular apatite. ν_3 PO_4 is the characteristic infrared absorption peak of acicular apatite crystals.[33,41]

The diffraction maxima from X-ray diffraction (Fig. 7B) indicate that the apatite nanocrystals were present in both types of mineralized lamellar mimetics. The main detection detected diffraction peaks matched well with those standard peaks of the acicular mineral ($Ca_{10}(PO_4)_6(OH)_2$) (JCPDS no. 09-0432),[42] data not shown. Interestingly, in the ethanolic Col-Ap lamellar mimetic, the *c*-axis (002) and (004) diffraction was stronger than the diffraction of HPAA Col-Ap lamellar mimetic, indicating that the acicular mineral was oriented along the *c*-axis and well crystallised.

Quantification of apatite content

Thermogravimetric analysis (TG/DTG) of the non-mineralized collagen matrix identified exothermic peaks attributed to three

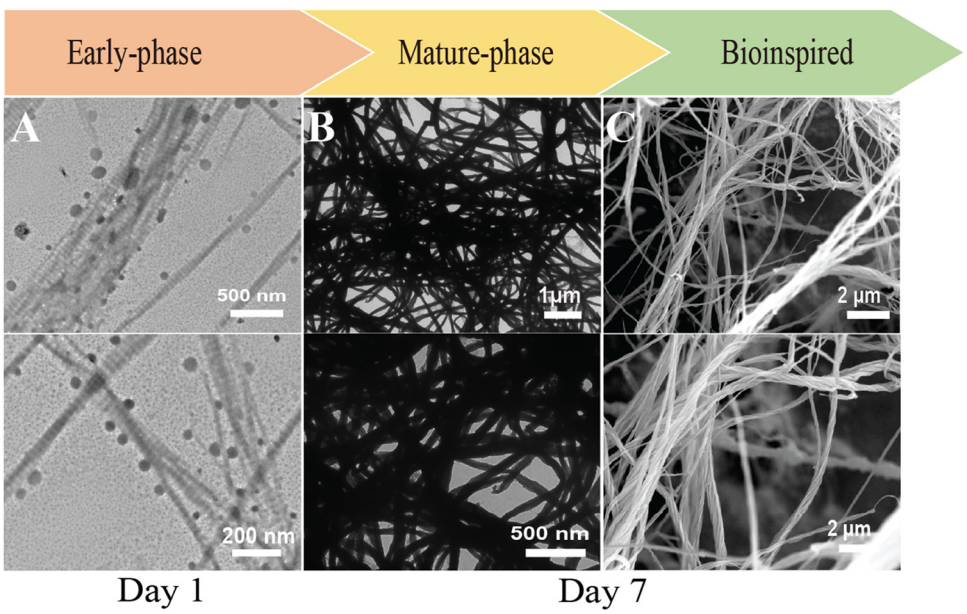

Fig. 5 Unstained conventional EM of hierarchical mineralization of on ethanolic Col-Ap mimetic construct. Induced *via* a biomimetic analog on collagen fibrils in the presence of ethanol depicting spatiotemporal events of early-phase (A) scale bar: 1 µm (top) and 500 nm (bottom) and (B) late-phase with hierarchical bundled-like arrangement of collagen mineralization. Scale bar: 1 µm (top) and 500 nm (bottom) and eventually resulting in mature heavily mineralized collagen fibrils. With the use of sequestration biomimetic analog amorphous ACP coacervates adsorbed within the fibrils (location in [(A)]), which later transforms into heavily mineralized intrafibrillar minerals, accentuating the braided microfibrillar hierarchical architecture of those collagen microfibrils with devoid cross-banding patterns. (C) FE-SEM micrograph depicts the rope-like morphology of the intra-interfibrillar mineralized ethanolic Co-Ap lamellar mimetic that were retrieved from the mineralisation assembly following 7 days of incubation. At high magnification (bottom), fibrillar collagen matrices became embedded with minerals and did not collapse upon drying. Scale bar 200 nm.

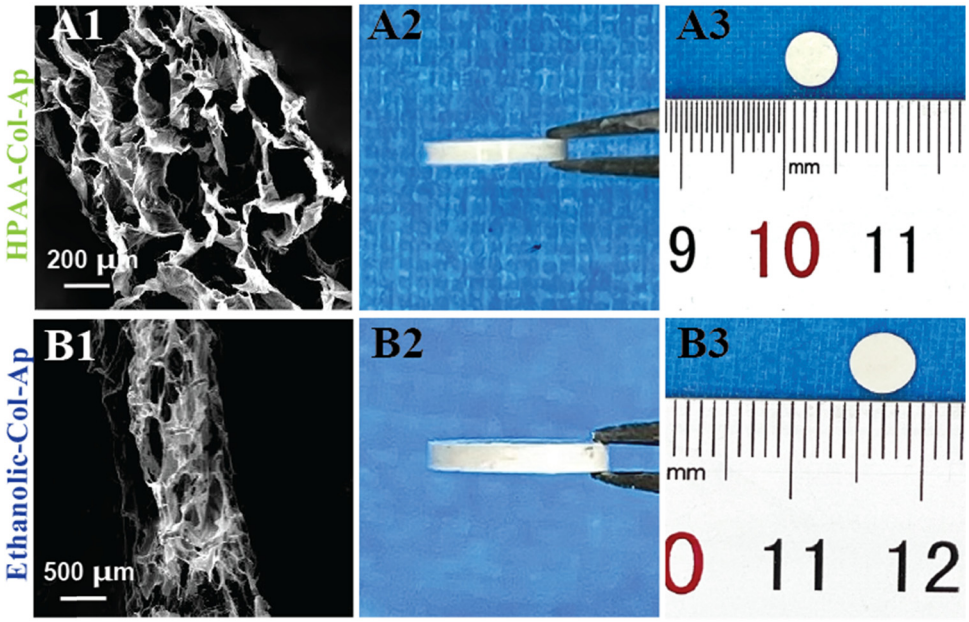

Fig. 6 Morphological characteristics of the different Col-Ap matrices. FE-SEM morphologies images of various unidirectional lamellar matrices produced *via* freeze-drying (A1) and (B1). Macroscopic representations of distinct dense lamellar composites (B2) and (B2).

distinct weight loss stages (Fig. 7C). The initial stage, observed between 30 and 100 °C, is ascribed to the evaporation of physically adsorbed water. A broad range of weight loss from 200 to 600 °C corresponds to the degradation (250–360 °C) and subsequent combustion (450–600 °C) of organic constituents. As the collagen's thermal decomposition shifted to higher temperatures, mineralized collagen matrices exhibited a higher decomposition/exothermic peak (increasing from 300 °C to 334 °C) compared to the collagen matrix. This upward shift indicates a robust structural integration between collagen and the mineral phase, implying that nanoscale mineral platelets are predominantly embedded within the intertwined collagen microfibrils. A minor weight loss occurring between 700 and 750 °C is likely due to the complete transition of the mineral phase into different phosphate forms.

Finally, the apatite content for the ethanolic Col-Ap lamellar mimetic is about 67.8 wt% (Fig. 7C, denoted in green), a value comparable to that of natural bone, which consists of roughly 65% mineral content and 25% collagen by weight, with the remaining portion being water.[33,43] However, the HPAA Col-Ap lamellar mimetic showed a lower mineral content of 40.6 wt% (Fig. 7C, denoted in pale blue), potentially because early extrafibrillar crystal formation impeded further infiltration into the collagen fibrils. Potentially, the early deposition of extrafibrillar crystals could have restricted further mineral infiltration into the collagen fibrils.

Moreover, the increase in residual weight percentage at 800 °C with prolonged mineralization in the artificially mineralized matrices (Fig. 7C) suggests that the incorporation of intra- and interfibrillar minerals continued throughout the PILP process.

Chemically modifying the core–shell liquid metal nanocapsule

In a typical experiment, after subjecting to ultrasonication (Fig. 8A), the EDS spectrum was analyzed, revealing peaks corresponding to Ga (78.98 wt%) and indium (20.59 wt%), which align with the anticipated values of the original material composition. This provides valuable insights into the stability of the particles (Fig. 8B and Fig. S3B, C, ESI†). Fascinatingly, the EDS spectra indicate that they possess a significantly lower quantity of oxygen (0.58 wt%) and an identified peak of sulfhydryl, which suggests that it is bound to the particle surface (refer to micrographs presented in (Fig. 8B)). Moreover, this results in transforming the parent metal into a compact sphere and causing aversion towards solid surfaces as evidenced by FESEM (Fig. 8C). Interestingly, the ruptured events triggered by ultrasonication causes oxide separation and this is best appreciated as large sheets as denoted by an asterix (Fig. S3A, ESI†). Under a closer view, the exclusivity of the oxide skin endows these particles with a rough surface (Fig. S3A, right, ESI†).[44] The existence of surface modification of the elemental EGaIn metal was determined by examining an isolated region of the nano-metal under high magnification TEM (Fig. 8D), where a distinct shell layer (oxide) formed on the capsule surface (denoted by a green arrow). Upon closer examination, thin tethers, presumably a PEG layer (indicated by the white arrow), were found extending from the surface of the EGaIn nanocapsule. Additional data, including a more intricate set of FESEM and TEM images, EDS mapping of individual elements and particle size distributions (DLS) from the analyzed samples, (Fig. S3, ESI†).

X-ray photoelectron spectroscopy (XPS) analysis was conducted on the Ga 3d transition region (Fig. 8E), revealing dual prominent peaks situated at binding energies of 20.6 eV and 18.4 eV. These spectral signatures were pivotal in quantifying the oxide layer thickness across different treatments. Zeta potential (electrophoretic mobility) measurement shows that the synthesized EGaIn nanocapsules with 1-dodecanethiol (DDT) has surface potential of −6.7 mV, while surface

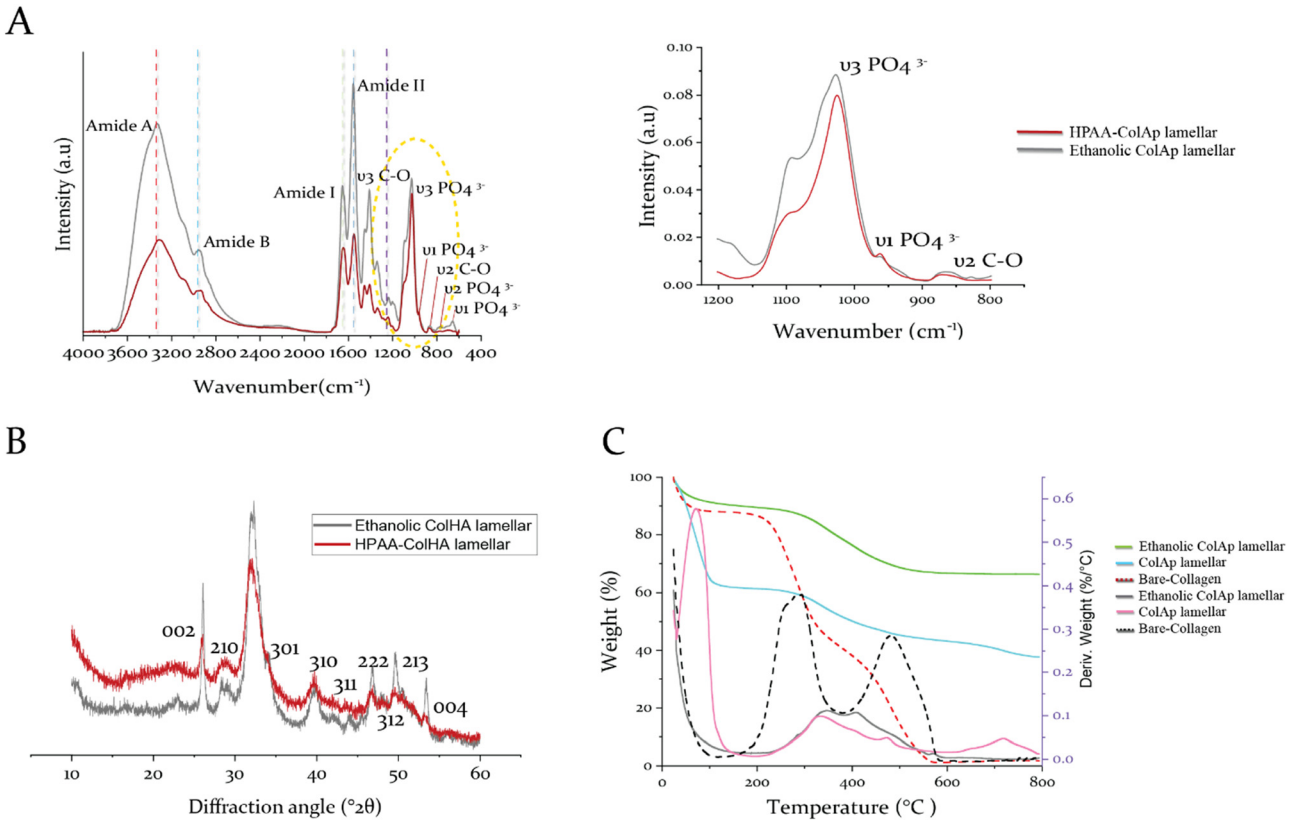

Fig. 7 Characterization of films obtained for HPAA Col-Ap lamellar and ethanolic Col-Ap lamellar mimetics. (A) Infrared spectra of HPAA Col-Ap lamellar mimetic (red) and ethanolic Col-Ap lamellar mimetic (dark-gray) incubated in solution for 1 week with spectral peaks of interest from 3600 to 400 cm^{-1}. The amide I (~1700–1600 cm^{-1}), II (~1580–1535 cm^{-1}), and III (~1200–1300 cm^{-1}) peaks are characteristic of type I collagen. The spectra of ethanolic Col-Ap lamellar mimetic (dark-gray) show increases in the amide A, B, I, II, and III peaks compared to the HPAA Col-Ap lamellar mimetic (red) indicating stronger intermolecular hydrogen bonding. (B) Showcases wide-angle X-ray diffraction image of the acicular mineral phase of both HPAA Col-Ap lamellar mimetic (red) and ethanolic Col-Ap lamellar mimetic (dark-gray). The peaks at 25.86–25.950 (°2θ) is characteristic of collagen sponge with diffraction peaks (002). The main peak at 31–39 (°2θ) is assigned to the convolution of four peaks 211, 112, 300 and 202 planes of the acicular apatite structure. (C) Showcases the thermogravimetric (TG/DTG) curves for both collagen lamellar matrices, mineralized for 7 days, *i.e.*, the ethanolic Col-Ap lamellar mimetic (green/gray) and the HPAA Col-Ap lamellar mimetic (pale blue/pink) indicating overall mineral contents of 67.8 wt% and 40.6 wt%, respectively, with four distinct derivative weight-loss peaks.

modification with PEG provides surface potential of +34.9 mV (Fig. 8F).

High content analysis of IMR-90 cells – EGaIn nanocapsules interactions

To overcome the colorimetric interference of PEG-EGaIn nanocapsules with toxicity assays, high-content imaging was used to determine cell toxicity, mitochondrial respiration and proliferation.[45] Fluorescence imaging of IMR-90 cells (Fig. 8G) indicated proliferation of the cells challenged with PEG-EGaIn nanocapsules at concentrations <0.75 g L^{-1}. Moreover, it was noted that higher concentration (1.0 g L^{-1}), significantly ($p < 0.0001$) alleviated the reduction in mitochondrial dynamics compared to the untreated. This effect is also reflected in the DNA content (Fig. 8H) where at 1.0 g L^{-1}, there was a significant drop in cell number. Previous studies investigating the cytotoxicity of gallium show a range of toxic concentrations that are comparable with the results in this study considering differing interaction times and cell lines.[46,47] After exposure of IMR-90 cells to PEG-EGaIn nanocapsules for 48 h (Fig. 8I), it is well known that mitochondrial membrane potential dynamics Ψ (MMP Ψ) is positively related to ATP production.

In accordance with ISO EN10993 – 5 criteria, the LDH enzyme release assay was employed to examine and evaluate the cytotoxicity effects of the samples. Specifically, when cells were in contact with a tested sample, if the cell vitality value was less than 70% of that of the negative control, it was indicative of potential cytotoxicity. At the end of 24 h exposure of IMR-90 cells to EGaIn nanocapsules (Fig. 8J), the results for <0.75 g L^{-1} PEG-EGaIn nanocapsules did not show definite LDH leakage (~10%) compared to the 1.0 g L^{-1} concentration (~50%) sample which had an increase in LDH release. For a positive control, the same number of IMR-90 cells were incubated with lysis buffer for 1 h before adding LDH testing solution.

Development and characterisation of hierarchical intrafibrillar apatite *via* nano-PEG-EGaIn-collagen matrix

Inspired by the outcome of biomimetic intrafibrillar mineralization of collagen lamellar matrices in the presence of benign-

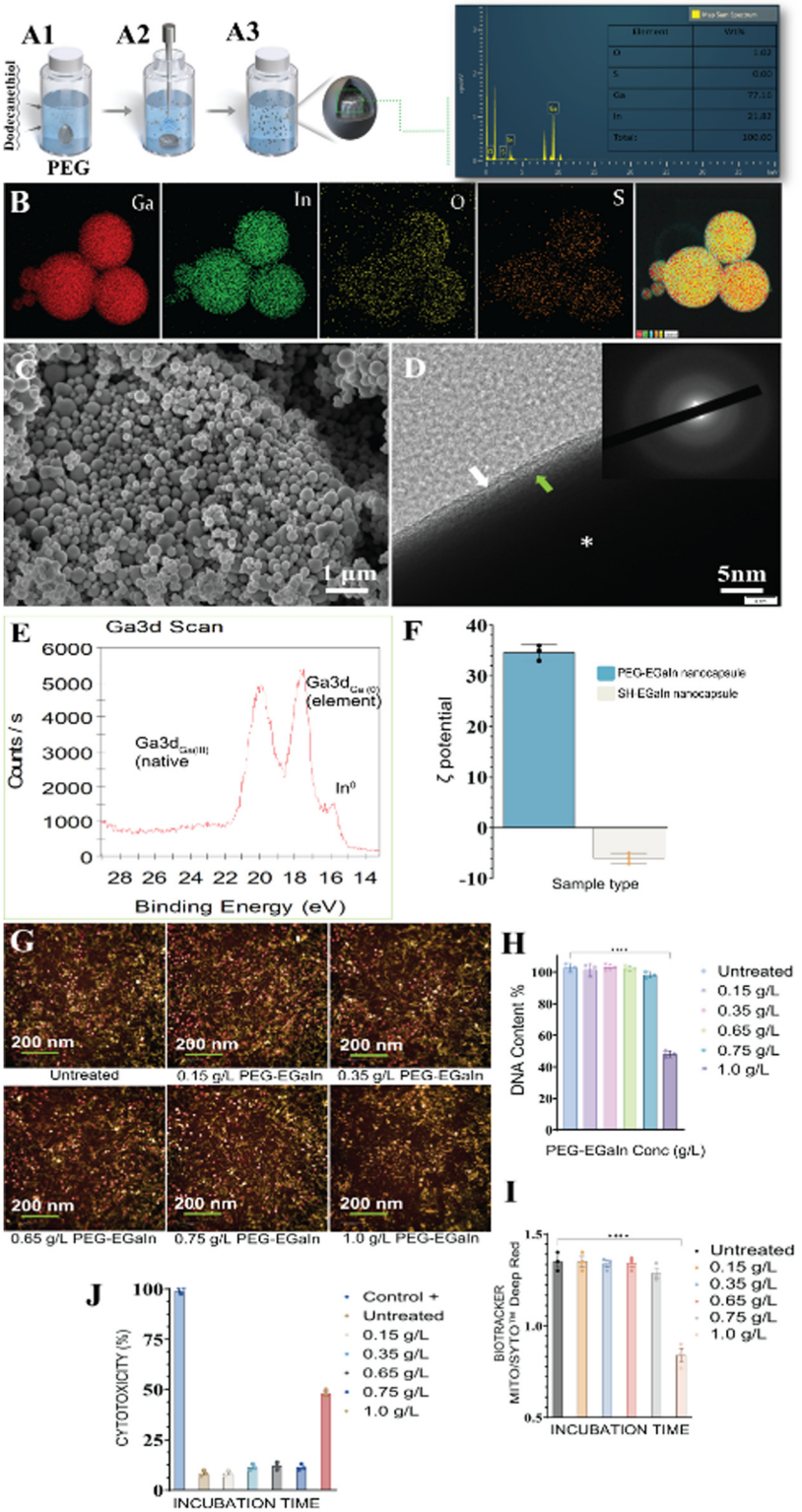

Fig. 8 Characterization of the functionalized EGaIn nanocapsules. (A1)–(A3) A schematic representation of the production of EGaIn nanocapsule suspension following sonication with TC. (B) EDS spectrum of PEG-EGaIn nanocapsules from (A) with corresponding signals to its field's metal; Sulfhydryl signal originating from DDT molecules bonded to the EGaIn metal surface. Scale bar 250 nm. (C) FESEM micrographs of PEG-EGaIn nanocapsules which are well-formed and show little evidence of oxidation and can be easily isolated for analysis by centrifugation. (D) High-magnification TEM image of an isolated PEG-EGaIn nanomaterial revealing a brighter amorphous shell of PEG (white arrow) and a tailored gallium oxide shell thickness (green arrow); also, the nanomaterial exhibited a darker amorphous core (asterix); SAED diffraction pattern is consistent with a liquid or amorphous phase (inset). (E) Representative XPS measurements for the Ga 3d region after colloid production. Peaks of interest are stated. (F) Zeta (ζ) potentials analysis of thiolated EGaIn and PEG-EGaIn nanocapsules. (G) IMR-90 cells were exposed to PEG-EGaIn nanocapsules (0.15, 0.35, 0.65, 0.75 and 1.0 g L^{-1}), stained with BioTracker 488 Green Mitochondia Dye and SYTO™ Deep Red following treatment period (72 h). (H) DNA content depicted by SYTO™ Deep Red from the captured fluorescence images. (I) Quantification of mitochondrial potential in IMR-90 cells at 48 h. (J) Cytotoxicity percentage LDH enzyme leakage in medium at 24 h. Data are presented as mean ± SEM and significance is denoted as ****$p < 0.0001$. Data were normalized with respect to untreated.

aqueous ethanol, we wished to introduce fibrillar collagen template immobilized with nano PEG-EGaIn metal since we found no literature on fabricating PEG-EGaIn nanocapsules mediated biomineralized composite that contains multiple levels of hierarchical organization (Fig. 9). High-magnification TEM image in Fig. 9A exhibits that the majority of PEG-EGaIn metal are embedded on the collagen matrix. The collagen matrix protects the embedded metal particles from coalescing and agglomeration thereby acting as a surfactant. It has been previously established that birefringence of collagen fibers can be observed through optical microscopy in polarization mode.[35,48] As depicted in (Fig. S5, ESI†), birefringence was noticeable for collagen in polarization mode in all situations owing to the intricate structure of the fibrils with 10 and 20% showcased collagen fibril formation, a stark contrast to 5% and untreated control. When examined with attenuated total reflection-Fourier transform infrared (ATR-FTIR) spectroscopy, PEG-EGaIn-col matrices had similar augmented amide I, II, and III peaks compared with bare collagen (Fig. 9B) with observed peaks attributed to the 1655–1670 cm^{-1} (amide I), 1551–1560 cm^{-1} (amide II), and 1241–1272 cm^{-1} (amide III). A characteristic C–O vibrations (augmented signatures from 1000 to

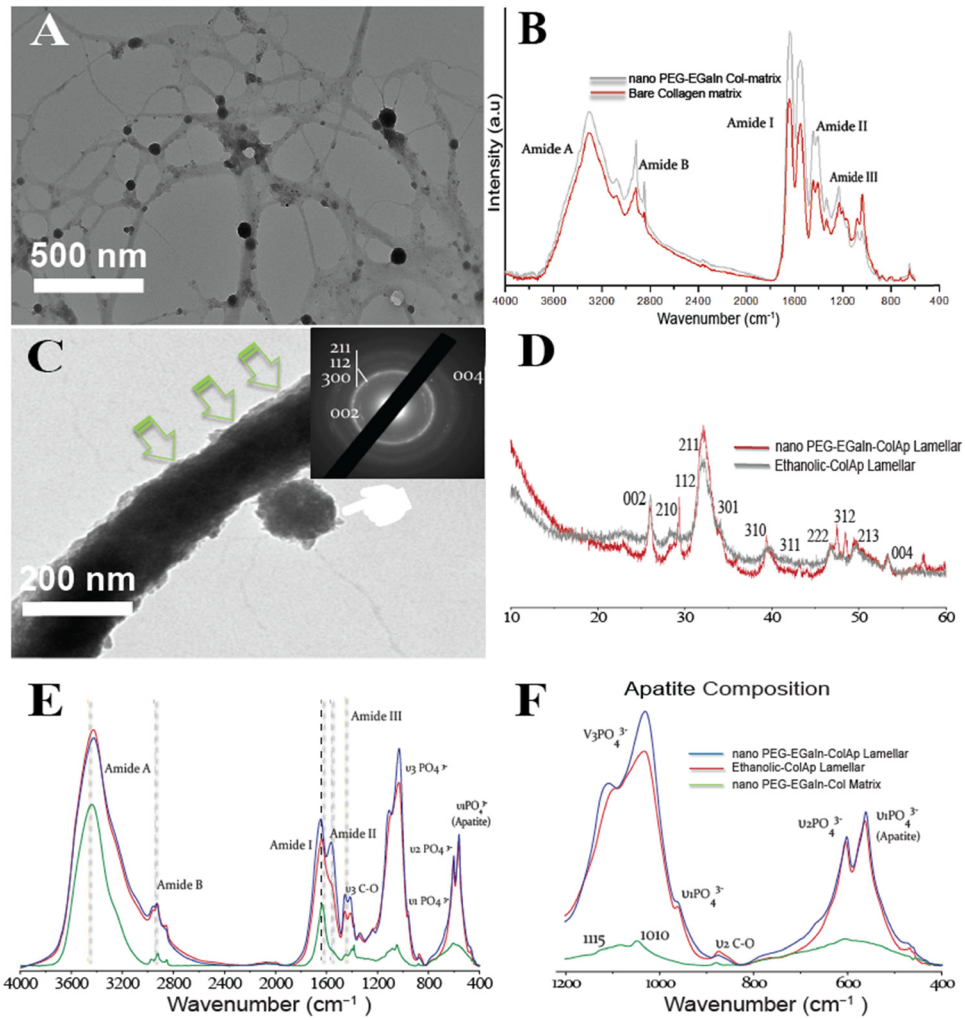

Fig. 9 Unstained conventional TEM tomography depicting late spatiotemporal events of intrafibrillar mineralization of PEG-EGaIn-Col-Ap mimetic. (A) EM tomography showcasing electron dense PEG-EGaIn nanocapsules that were spatially distributed throughout the bundled collagen matrices (PEG-EGaIn-col matrices). Scale bar: 500 nm. (B) Infrared absorption spectra of the sbare collagen matrix (red) and nano PEG-EGaIn col-matrix (grey). Spectra peaks were normalized along the amide bands of bare-collagen matrices. Compared to the spectrum of PEG-EGaIn-col matrices, the backbone confirmation of collagen was preserved. (C) High magnification, TEM micrograph reveals a hierarchical assembly of mineral nanoplatelets in PEG-EGaIn-Col-Ap microfibrils, with corresponding SAED patterns showing mineral arrangements and diffraction signatures matching crystalline apatite. [(inset from (C))] reveals hierarchical arrangement of the minerals along the long axis (arc-shaped patterns distinctive to collagen signature along the 002 and 004 diffraction planes). The apparent continuous ring patterns corresponds to the acicular nanoplatelets with (1122), (211), (300) and (310) diffraction signatures. (D) Wide-angle X-ray diffraction of the crystalline apatite phase in the ethanolic-Col-Ap mimetic (grey) and PEG-EGaIn-Col-Ap matrices (red). (E) Infrared spectra of PEG-EGaIn-col matrices (green), ethanolic-Col-Ap (red) and PEG-EGaIn-Col-Ap matrices (blue) incubated in solution for 1 week. (F) Immobilization with EGaIn nanocapsules, spectroscopical functionalities of the chemically modified nano-PEG-EGaIn col-matrix (high magnification from (E) still led to the heavy intrafibrillar mineralisation of the collagen fibrils with spectral peaks of nanoplates at 600 and 560 cm^{-1}).

1100 cm^{-1}) that is ascribed to either hydroxyproline or from glycosidic side chain distinct to bare collagen matrix indicates that collagen conformational backbone was preserved (augmented signatures at 1032 and 1082 cm^{-1}) and remains in the native structure.

Moreover, intrafibrillar mineralization from individual microfibril template immobilized with nano-PEG-EGaIn, had a discrete hierarchical arrangement of the mineral platelets that were more heavily stacked along the gap zones of the fibrillar assembly revealing a faint cross-banding periodicity and with orientation along the fibril's *c*-axis (Fig. 9C; SAED inset), reproducing the hierarchical nanostructure of the native bone. Interestingly, PEG-EGaIn nanocapsules still appeared to be periodically spaced along the fibril surface (Fig. 9C and Fig. S3B, S6B, ESI†). The spectroscopical kinetics from retrieved specimens (day 7): biomimetic ethanolic-Col-Ap, PEG-EGaIn-Col-Ap and PEG-EGaIn-col matrices (serving as the template) were examined under attenuated total reflection-Fourier transform infrared (ATR-FTIR) spectroscopy (Fig. 9E and F) whereas the former specimens were used to determine the apatite/collagen ratios. For the typical PEG-EGaIn-col matrices, ATR-FTIR peaks at ~1700 to 1600 cm^{-1} were assigned to the amide I (C═O stretching), deformations of both amide II (NH bend coupled with CN stretching) and amide III (NH bend coupled with CN stretching) were observed at ~1580–1535 cm^{-1} and ~1200–1300 cm^{-1} respectively. Along with the organic components, the vibrations of PO_4^{3-} groups (ν_1, ν_2 and ν_3 PO_4 stretching modes) appeared at 960, 1100 and 1038 cm^{-1}. However, when examined, there was a discernible increase in these characteristic peaks, which may be attributed to the nucleation inhibitor and not the PEG-EGaIn nanocapsules since the ultrastructure of the collagen matrix was preserved. However, with the formation of the nanoapatite, there was a marked alteration of the PO_4^{3-} group with vibration bands at 1010 cm^{-1} and 1115 cm^{-1} (ν_1 and ν_3 PO_4 stretching modes) (Fig. 9F) corresponding to similar interactions in the literature. The mineral kinetics of the mineralised collagen lamellar matrices was noted by splitting of a single peak at 560 and 604 cm^{-1} (Fig. 9F) characteristics of apatite (ν_4 and ν_2 PO_4^{3-} bending vibration). Peaks at 873 (ν_2 C–O stretching mode) and 1413 cm^{-1} (ν_3 C–O bending mode) were assigned to the carbonate substitution in the apatite lattice, respectively. Also, decrease in 870 cm^{-1} vibrations revealed ethanol evaporation resulting to the calcium carbonate formation. The results indicate that even after amalgamation with liquid-metal nanocapsules, spectroscopical functionalities of the chemically modified collagen matrices still led to the heavy mineralisation of the braided collagen microfibrils.

Discussion

The results presented here demonstrate a biomimetic approach to design a PEG-EGaIn-Col-Ap matrix. Inspired by the ethanolic-Col-Ap matrix complex, we created a dual-functional biomimetic (PEG-EGaIn-Col-Ap matrices) using a versatile synthetic procedure by tailoring the collagen template architecture incorporated with the PEG-EGaIn nanocapsule into the Col-Ap mimetic. In our system, collagen matrices mineralized with ethanolic dispersions containing PEG-EGaIn nanocapsules ($\leq$20%, v/v) achieved pure hierarchical intrafibrillar biomineralization, indicating that the in mineral precursor binding capacities would not lead to different outcomes while in the presence of benign-aqueous ethanolic-prenucleation inhibitors (submitted manuscript), but the ''gatekeeper'' could determine infiltration of fluid-like ACP nano precursors to be oriented through it.

It has been proposed that the kinetic stability of collagen in the presence of ethanol (<40%) ethanol concentration at elevated temperatures had a destabilizing effect on the collagen structure.[14] In our current study, we were successfully able to achieve hierarchical intrafibrillar biomineralization in the presence of benign-aqueous-ethanol (ethanolic-Col-Ap) and mineral inhibitors that closely matches that of bioinspired bone (submitted manuscript). Therefore, to avoid the pitfalls of structural defect on the collagen ultrastructure, we chose $\leq$20% ethanol where collagen–ethanol schema (with-or-without PEG-EGaIn nanocapsules) upon mineralization, would preserve the intrafibrillar structures of the membranes. In Fig. 1 of Scheme 1 schematically depicts this ''inchoate'' stage of mineralization, which is seen at high magnification in Fig. 1 and has the unique characteristic of reproducing the microfibrillar subunits of a collagen fibril.[49] Similar results were reported when high-molecular weight polyacrylic acid (HPAA), a biomimetic analog was used to surrogate NCP function as selective inhibitors, where reconstituted, single collagen fibrils were remineralized.[36,50] Comparing our current findings with the excellent research of these research groups allows us to draw important conclusions even though the two studies were not identical. The fluidic ACP nano precursors described above are called polymer-induced liquid precursors by Gower and her colleagues, who first studied polyanionic acid stabilized amorphous calcium carbonate phases.[33,34,51] HPAA can sequester the ACP phases by controlling the dimensions into droplets smaller than the wavelength of light, giving the appearance of transparency to the unaided eye.[52] Because the prenucleation clusters (ACP) are surrounded by a low molecular weight biomimetic analog layer that most likely acts as a surfactant,[52] ACP nano precursors can be isolated from the benign aqueous ethanol biomineralization medium by liquid–liquid phase.[15] This allows individual amorphous ACP nanodroplets to coacervate, penetrate and forms a continuous phase within the braided collagen fibril (see Scheme 1B, C and Fig. 1B).[34,51]

These roughly 50–300 nm-diameter amorphous globular bodies adjacent to the braided fibrils are depicted in Fig. 1 and Fig. S1, S2 (ESI†) seem to coalesce and grow in agglomeration further supporting previous discussions on amorphous globular body agglomeration.[53–55] Particularly intriguing is the amorphous structure depicted in Fig. 1B, 2B, 4A and Fig. S2 (ESI†), which had appendages appearing to be in contact with a collagen fibril that had the electron-dense continuous, braided mineral phase infiltrated within it. Scheme 1B and C, provides

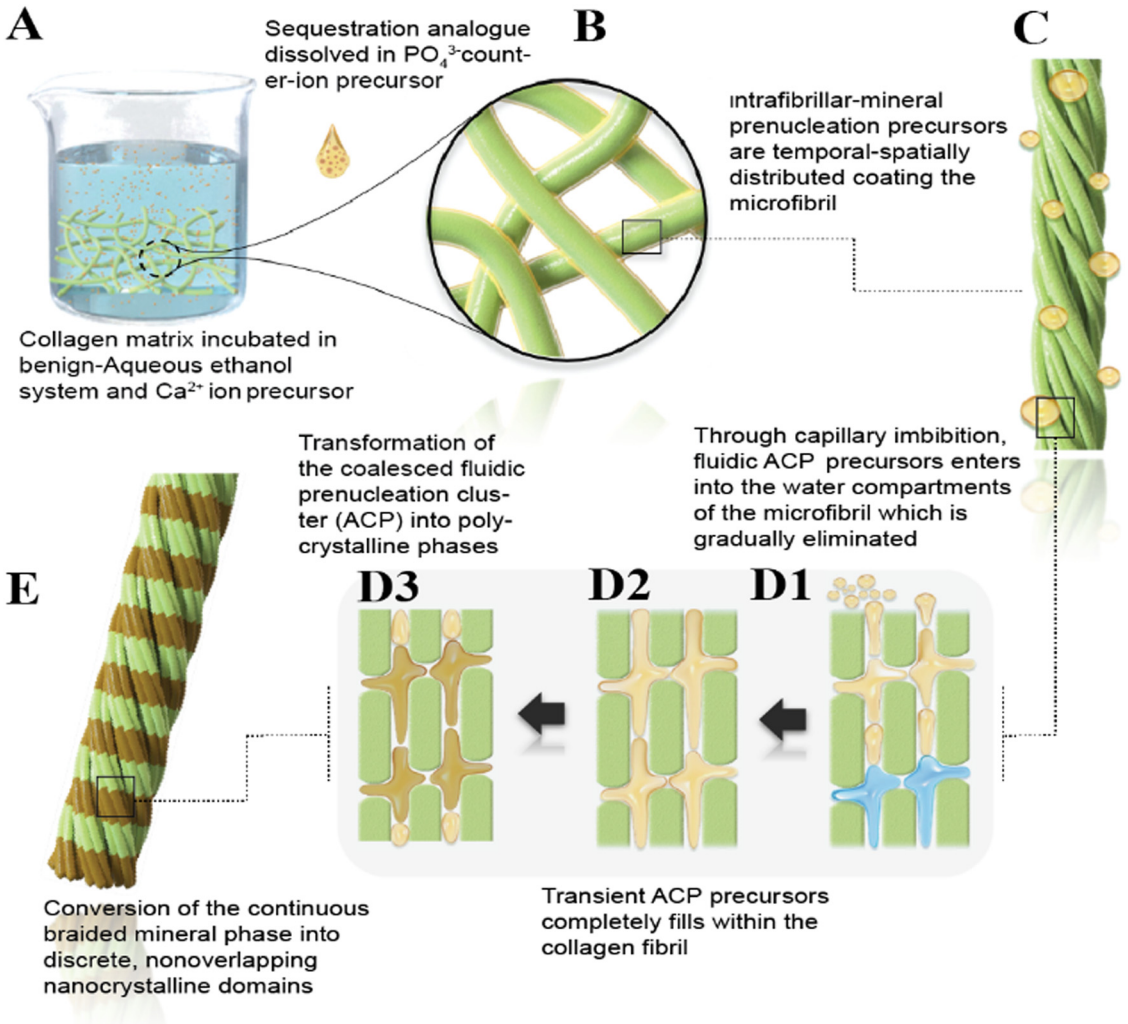

Scheme 1 (A) Schematic summarizing the features of biomimetic intrafibrillar mineralization observed with the infiltration of ethanol molecules into the hydrated collagen matrices. (A) Collagen matrix mineralization was performed according to the PILP method in the presence of benign-aqueous ethanol system. (B) A representative example of moderately high magnification view of (A) depicting a rope-like microfibril-continuous amorphous phase and the surrounding solution are divided by a distinct phase boundary. (C) A representative example of a high magnification view, taken from (B) showcases the PILP phase of electron-dense globular bodies adjacent to the rope-like microfibril. (D_1) Moderately high magnification view of (C) showcasing both prenucleation clusters and polymer-stabilized amorphous nanoprecursors adsorb on the braided collagen microfibril (positively charged C-pro-peptide), and due to their fluidic character, become imbibed into the interstitial spaces of the collagen microfibril by capillary action. Ethanol molecules infiltrated into collagen fibrils only in the gap region and not into the overlapped regions displacing the free water within the collagen fibrils. The liquid-like ACP nanoprecursor displaces loosely bound water within the braided collagen microfibril. (D_2) The collagen fibril becomes fully imbibed and coalescence of individual nanodroplets of amorphous mineral precursor. (D_3) During the onset of intrafibrillar mineral deposits, there is a lack of long-range structural order. The crystallographically disordered intrafibrillar minerals interact with the intrafibrillar niche owing to the confinement of the metastable amorphous nanoprecursors inside the interstitial spaces. (E) A hypothetical depiction of rope-like collagen microfibril embedded with mineral nanoplatelets.

a schematic representation of these features. While it may have been coincidental, these amorphous globular structures were observed in this study. These transient, metastable amorphous bodies are usually difficult to identify unless certain techniques such as cryogenic-EM[50,56] or dynamic light scattering are applied.[57] It is possible that their entanglement in the polymer matrix enabled the identification of these droplets during our investigations. This is comparable to the outcomes of a previous study, which used PAA-stabilized apatitic nanospheres scattered throughout a nanocomposite's PAA-matrix.[52] According to more previous studies, even smaller (0.6–1.1 nm) amorphous prenucleation ionic clusters may have aggregated to form these fluidic ACP nano precursors[53–55,58–60] related to their surface energy or volumetric Gibbs free energy.[61] The nonclassical crystallization theory proposes that the first two-step nucleation model of a kinetically driven stairway of events

that reduces activation-energy barriers during a crystallization event[61–65] may be prenucleation clusters and polymer-stabilized amorphous nanodroplets. With the observation of intrafibrillar mineralization in our current ethanol system, it is more likely that sequestered fluidic ACP nano precursors instead of water occupied the internal environment of those collagen fibrils. The loosely bound water in the collagen molecules and the free water in the fibrils would need to be replaced with fluidic ACP nano precursors to mineralize the collagen fibrils (see Scheme $1D_1$, Fig. 1B, 2B, and Fig. S2B, ESI†).[15] Previous studies found that the water in the collagen fibrils was replaced with amorphous calcium phosphate precursors, which led to a decrease in water molecular mobility as shown by a decrease in water proton transverse (T2) relaxation times.[15,66] Thus, one could consider the intrafibrillar mineralization of collagen fibrils to be a dehydration process.

Ethanol effectively removes free and some loosely bound water from the collagen matrix, allowing closer packing of collagen molecules.[7,67] This process potentially improves the infiltration of ACP nano precursors, which are otherwise hindered by the presence of water (*i.e.*, gatekeeper) and the HPAA. It is reasonable to argue that this dehydration process alters the size-exclusion properties of the collagen matrix and bound HPAA-ACP, allowing ACP nano precursors to penetrate more deeply into the aqueous compartments while excluding larger molecules, which could potentially improve the mechanical properties of the collagen-mineral interface.[16,68] In this study, several segments of the same collagen fibrils displayed evidence of template-directed transformation into polycrystalline phases from the coalesced amorphous precursor phase (Fig. 1B, 2B and Fig. S2, ESI†) and this is depicted schematically in Scheme $1D_2$, D_3 and E. These nanocrystalline domains eventually form into oriented single crystals after being stabilized by the template molecules.[69] However, in this biomimetic analog model (Fig. 1A, 2A and 3), analogs with higher molecular weights are bound to discrete sites along the collagen surface and are said to suppress the infiltration of ACP precursors into the aqueous compartments of the collagen fibril.[36,42,50] This contributes to the understanding of why the gap zones in collagen fibrils initially contain apatite platelets through heterogeneous "charge patches" (Fig. 3B).[70] Although corroborated experimental evidence is difficult to obtain, the authors of a previous study observed that ethanol molecules were found to infiltrate the intermolecular spacing in the gap region of the collagen but not in the overlap region providing some support for the above hypothesis.[15]

Mesoscopic transformation is the term used to describe this bottom-up, polymer- or protein-dependent assembly of nanocrystalline domains into single crystals. Gower and her team successfully produced crystals with unique morphological characteristics, such as extruded mineral fibers,[71,72] mineralized collagen composites, and calcium carbonate crystalline aggregates that replicate the microporous structure of sea urchin spines.[73] In subsequent research, they created intrafibrillar mineralization of collagen fibrils using polyaspartate-stabilized calcium phosphate (CaP) precursors.[72] They suggested that the charged polymer acts as a process-directing agent, forming a fluidic amorphous calcium phosphate (ACP) precursor. This precursor is drawn into the collagen fibrillar interstitial spaces by capillary action and subsequently solidifies and crystallizes into the more thermodynamically stable apatite phase upon dehydration.[72]

The experiment's most pronounced example of this sequence of events is the continuously braided mineral phase's development into distinct, nonoverlapping nanocrystals (Fig. 4B, D, E and 9C) and, based on the sectioning plane, showcases a hypothetical depiction of intrafibrillar biomineralization where nanoscopical mineral platelets are confined within the braided collagen microfibrils (Scheme 1E). Electron microscopy observations alone are not sufficient to verify mesoscopic transformation. Indirect evidence, however, might come from comparing the continuous braided mineral phase configuration with the post-transformation overlapping platelet phase visible in the TEM images. In Smith's microfibril model,[74] a bundle of five intertwined triple-helical collagen molecules was packed into microfibrillar subunits inside a collagen fibril. Holmes *et al.* estimate that about 3900 collagen molecules would be present in a cross-section of a collagen fibril with a diameter of 100 nm;[75,76] this is the same as 780 microfibrils in a collagen fibril with a diameter of 100 nm. In fact, a longitudinal section through a collagen fibril that was infiltrated by the continuously braided electron-dense mineral nanocrystallites (Fig. 5B, C and Fig. S6, ESI†) seemed to corroborate the idea that the collagen fibril contained a significant number of microfibrils. When compared to the more mature platelets shown in (Fig. 3B), the dimensions of these nanocrystalline phases were noticeably smaller (Fig. 4E). The mesoscopic transformation of the amorphous mineral phase into larger crystallites after its initial condensation into metastable prenucleation ion clusters (Fig. 1B) is the only explanation for the observed reduction of the number of electron-dense strands to the number of nanoplatelets in the mature mineralized fibrils (Fig. 4E). The bottom-up, template-directed, particle-based mechanism of metastable nanocomponent assembly into single crystalline structures seems to be supported by these observations.[10,55,77,78]

Having demonstrated and discerned the differences in the quality of the highly hierarchical assembly of intra-interfibrillar mineralization by bare collagen mineralized with biomimetic analogues and benign-aqueous ethanol *via* contemporary EM, this alone is incapable of truly explaining the kinetic changes in the intra-interfibrillar environment on the collagen matrices ultrastructure, which might be resolved *via* molecular dynamic simulation.[15] The collagen–ethanol system may offer insights into the ability to cache apatite mineral precursors for intrafibrillar mineralization in the early-late stages of mineralization. Moreover, these observations highlight the significant impact of ethanol on the mineralization process of collagen, which could be crucial for applications in biomaterials and tissue engineering.

In the realm of biomimetic designs, there has been a notable paradigm shift that has drawn significant attention, focusing on the development of flexible metals possessing reduced cytotoxicity and augmented bone-regenerating capabilities. In the present study, we explored the impacts of varying

concentrations of PEG-EGaIn nanocapsules on cytocompatibility with respect to IMR-90 cells. The findings from *in vitro* cytotoxicity and proliferation assays indicated a favorable performance of the PEG-EGaIn nanomaterials. The data obtained from high-content imaging and corresponding signal quantifications demonstrated an increase in metabolic activity based on mitochondria respiration and proliferation by quantifying the DNA content in cells treated with <0.75 g L^{-1} PEG-EGaIn nanocapsule concentrations. However, a significant shift in the impact on mitochondrial health and toxicity was noticeable at 1.0 g L^{-1} concentration.

In summary, the present model of intrafibrillar mineralization enhancement by benign-aqueous ethanol provides strong support for future investigations on site-specific intra-interfibrillar mineralization mechanisms. Moreover, the presence of benign-aqueous ethanol did not seem to repress acicular minerals that are randomly aggregated within the gap zones of the fibrillar collagen. Interestingly, benign-aqueous ethanol demonstrates an intriguing capability to enhance the concentration of ACP precursors, thereby promoting more effective intrafibrillar mineralization. This stands in contrast to water-mediated conditions (control group). In the latter scenario, a biomimetic approach *via* HPAA resembling fetuin and osteopontin was used,[79] with molecular masses exceeding 40 kDa. As posited by the size exclusion theory, these proteins are predominantly found on the surface of collagen fibrils.[68]

It is evident from this study that the fibrillar collagen template (acting as a surfactant) controlled nanoscale PEG-EGaIn nanocapsules from coalescing and hindering their agglomeration. Also, immobilization of PEG-EGaIn metal did not seem to repress apatite nanoplatelets that are randomly aggregated within the gap zones of the fibrillar collagen. With the use of Col immobilized PEG-EGaIn nanocapsules, it is expected that ceramics of biological interest may be produced under very economically friendly conditions with the morphology mimicking the fibrous Col with strong mechanical properties, totally different from previous reports.[31,80] Also, mimicking biological processes or utilizing some of their components in molecularly well-defined fibers may result in the modification of implant surfaces with highly desirable properties. We anticipate that our biomimetic material and design concept can be used to inspire application towards hard tissue engineering as well as provide insights into intersections of mechanisms in biomimetic mineralization.

Thus, our study provides new insights into the suitability of PEG-EGaIn nanocapsules with IMR-90 cells as it satisfies the basic requirement of an ideal implant biomaterial. With the limitation of the study, we have already done a comprehensive overview of methods assessing the biocompatibility of these nanomaterials with rBMSCs and *in vivo* material–tissue interactions induced by PEG-EGaIn-Col-Ap lamellar mimetic. Our previous study showed that the PEG-EGaIn nanocapsules promoted osteogenic differentiation of rBMSCs, giving confidence to their ability to promote long-term defect healing *in vivo* [under peer-reviewed revision, co-author Y. Qu] which is consistent with the findings of this study.

Author contributions

K. H. M. and Y. Q. conceptualized the main idea of the project and performed research. S. T. prepared the figure arrangements. X. S., L. Z., and X. W. supervised the project and reviewed the manuscript.

Data availability

The data used to support the findings of this study are included within the article.

Conflicts of interest

The authors declare that they have no competing interests.

Acknowledgements

This work was supported by the National Key R&D Program of China (No. 2023YFC2412300), the Key R&D Program in Shandong Province (No. 2019JZZY011106) and in part, a Chinese Government Scholarship.

References

1 F. Nudelman and N. A. Sommerdijk, Biomineralization as an inspiration for materials chemistry, *Angew. Chem., Int. Ed.*, 2012, **51**(27), 6582–6596.
2 A. Boskey, Biomineralization: Conflicts, challenges, and opportunities., *J. Cell. Biochem.*, 1998, **72**, 83–91.
3 Q. Wang, *et al.*, Expanding from materials to biology inspired by biomineralization, *Interdiscip. Mater.*, 2024, **3**(2), 165–188.
4 F. Nudelman and N. A. J. M. Sommerdijk, Biomineralization as an inspiration for materials chemistry, *Angew. Chem.*, 2012, **51**(27), 6582–6596.
5 E. Beniash, Biominerals–hierarchical nanocomposites: the example of bone, *Wiley Interdiscip. Rev.:Nanomed. Nanobiotechnol.*, 2011, **3**(1), 47–69.
6 L. C. Palmer, *et al.*, Biomimetic systems for hydroxyapatite mineralization inspired by bone and enamel, *Chem. Rev.*, 2008, **108**(11), 4754–4783.
7 L. Gonzalez, *et al.*, Effects of isopropanol on collagen fibrils in new parchment, *Chem. Central J.*, 2012, **6**, 24.
8 H. S. Gupta, *et al.*, Cooperative deformation of mineral and collagen in bone at the nanoscale, *Proc. Natl. Acad. Sci. U. S. A.*, 2006, **103**(47), 17741–17746.
9 A. Veis and J. R. Dorvee, Biomineralization mechanisms: a new paradigm for crystal nucleation in organic matrices, *Calcif. Tissue Int.*, 2013, **93**(4), 307–315.
10 F. Nudelman, *et al.*, The role of collagen in bone apatite formation in the presence of hydroxyapatite nucleation inhibitors, *Nat. Mater.*, 2010, **9**(12), 1004–1009.
11 W. J. Landis and R. Jacquet, Association of calcium and phosphate ions with collagen in the mineralization of vertebrate tissues, *Calcif. Tissue Int.*, 2013, **93**(4), 329–337.

12 H. Cölfen, Biomineralization: A crystal-clear view, *Nat. Mater.*, 2010, **9**(12), 960–961.
13 L. Salvatore, *et al.*, Mimicking the Hierarchical Organization of Natural Collagen: Toward the Development of Ideal Scaffolding Material for Tissue Regeneration, *Front. Bioeng. Biotechnol.*, 2021, **9**, 644595.
14 A. Gopinath, *et al.*, Effect of aqueous ethanol on the triple helical structure of collagen, *Eur. Biophys. J.*, 2014, **43**(12), 643–652.
15 S. E. Jee, *et al.*, Investigation of ethanol infiltration into demineralized dentin collagen fibrils using molecular dynamics simulations, *Acta Biomater.*, 2016, **36**, 175–185.
16 A. Chiba, *et al.*, The effects of ethanol on the size-exclusion characteristics of type I dentin collagen to adhesive resin monomers, *Acta Biomater.*, 2016, **33**, 235–241.
17 N. Ilyas, A. C. Cook and C. E. Tabor, Designing Liquid Metal Interfaces to Enable Next Generation Flexible and Reconfigurable Electronics, *Adv. Mater. Interfaces*, 2017, **4**, 1700141.
18 J. H. Kim, *et al.*, Cytotoxicity of Gallium-Indium Liquid Metal in an Aqueous Environment, *ACS Appl. Mater. Interfaces*, 2018, **10**(20), 17448–17454.
19 Y. Lin, *et al.*, Shape-transformable liquid metal nanoparticles in aqueous solution, *Chem. Sci.*, 2017, **8**(5), 3832–3837.
20 S. A. Chechetka, *et al.*, Light-driven liquid metal nanotransformers for biomedical theranostics, *Nat. Commun.*, 2017, **8**, 15432.
21 Y. Lu, *et al.*, Transformable liquid-metal nanomedicine, *Nat. Commun.*, 2015, **6**, 10066.
22 R. Liu, *et al.*, Transformable Gallium-Based Liquid Metal Nanoparticles for Tumor Radiotherapy Sensitization, *Adv. Healthcare Mater.*, 2022, **11**(11), e2102584.
23 N. J. Morris, Z. J. Farrell and C. E. Tabor, Chemically modifying the mechanical properties of core–shell liquid metal nanoparticles, *Nanoscale*, 2019, **11**(37), 17308–17318.
24 J. Liu and L. Yi, Preparations and Characterizations of Functional Liquid Metal Materials, in *Liquid Metal Biomaterials: Principles and Applications*, ed. J. Liu and L. Yi, Springer Singapore, Singapore, 2018, pp. 95–115.
25 Y. Liu, *et al.*, Hierarchical Intrafibrillar Nanocarbonated Apatite Assembly Improves the Nanomechanics and Cytocompatibility of Mineralized Collagen, *Adv. Funct. Mater.*, 2013, **23**, 1404–1411.
26 L. Yu, *et al.*, Enhanced Intrafibrillar Mineralization of Collagen Fibrils Induced by Brushlike Polymers, *ACS Appl. Mater. Interfaces*, 2018, **10**(34), 28440–28449.
27 C. Hu, L. Yu and M. Wei, Biomimetic intrafibrillar silicification of collagen fibrils through a one-step collagen self-assembly/silicification approach, *RSC Adv.*, 2017, **7**(55), 34624–34632.
28 L. Yu, *et al.*, Intrafibrillar Mineralized Collagen-Hydroxyapatite-Based Scaffolds for Bone Regeneration, *ACS Appl. Mater. Interfaces*, 2020, **12**(16), 18235–18249.
29 D. K. Khajuria, *et al.*, Accelerated Bone Regeneration by Nitrogen-Doped Carbon Dots Functionalized with Hydroxyapatite Nanoparticles, *ACS Appl. Mater. Interfaces*, 2018, **10**(23), 19373–19385.
30 Y. Song, *et al.*, Zinc Silicate/Nano-Hydroxyapatite/Collagen Scaffolds Promote Angiogenesis and Bone Regeneration via the p38 MAPK Pathway in Activated Monocytes, *ACS Appl. Mater. Interfaces*, 2020, **12**(14), 16058–16075.
31 S. Aryal, *et al.*, Immobilization of collagen on gold nanoparticles: preparation, characterization, and hydroxyapatite growth, *J. Mater. Chem.*, 2006, **16**(48), 4642–4648.
32 K. H. Svendsen and M. H. Koch, X-ray diffraction evidence of collagen molecular packing and cross-linking in fibrils of rat tendon observed by synchrotron radiation, *EMBO J.*, 1982, **1**(6), 669–674.
33 M. J. Olszta, *et al.*, Bone structure and formation: A new perspective, *Mater. Sci. Eng., R*, 2007, **58**(3), 77–116.
34 L. B. Gower, Biomimetic model systems for investigating the amorphous precursor pathway and its role in biomineralization, *Chem. Rev.*, 2008, **108**(11), 4551–4627.
35 H. Yoshikawa, *et al.*, Effects of alcohol on the solubility and structure of native and disulfide-modified bovine serum albumin, *Int. J. Biol. Macromol.*, 2012, **50**(5), 1286–1291.
36 Y. Liu, *et al.*, Hierarchical and non-hierarchical mineralisation of collagen, *Biomaterials*, 2011, **32**(5), 1291–1300.
37 G. Shanmugam, *et al.*, 2,2,2-Trifluoroethanol disrupts the triple helical structure and self-association of type I collagen, *Int. J. Biol. Macromol.*, 2013, **54**, 155–159.
38 D. B. Burr, The contribution of the organic matrix to bone's material properties, *Bone*, 2002, **31**(1), 8–11.
39 C. H. Yoder, *et al.*, Structural water in carbonated hydroxylapatite and fluorapatite: confirmation by solid state (2)H NMR, *Calcif. Tissue Int.*, 2012, **90**(1), 60–67.
40 D. J. Hulmes, *et al.*, Radial packing, order, and disorder in collagen fibrils, *Biophys. J.*, 1995, **68**(5), 1661–1670.
41 Y. Liu, *et al.*, Intrafibrillar collagen mineralization produced by biomimetic hierarchical nanoapatite assembly, *Adv. Mater.*, 2011, **23**(8), 975–980.
42 Y. K. Kim, *et al.*, Mineralisation of reconstituted collagen using polyvinylphosphonic acid/polyacrylic acid templating matrix protein analogues in the presence of calcium, phosphate and hydroxyl ions, *Biomaterials*, 2010, **31**(25), 6618–6627.
43 J. D. Currey, *Bones: Structure and Mechanics*, 2002.
44 J. N. Hohman, *et al.*, Directing substrate morphology via self-assembly: ligand-mediated scission of gallium-indium microspheres to the nanoscale, *Nano Lett.*, 2011, **11**(12), 5104–5110.
45 A. R. Collins, *et al.*, High throughput toxicity screening and intracellular detection of nanomaterials, *Wiley Interdiscip. Rev.:Nanomed. Nanobiotechnol.*, 2016, **9**(1), e1413.
46 M. Kurtjak, *et al.*, Biocompatible nano-gallium/hydroxyapatite nanocomposite with antimicrobial activity, *J. Mater. Sci.: Mater. Med.*, 2016, **27**(11), 170.
47 S. Cheeseman, *et al.*, Assessment of the Cytotoxicity of Nano Gallium Liquid Metal Droplets for Biomedical Applications, *ACS Appl. Nano Mater.*, 2022, **5**(11), 16584–16593.
48 H. P. Singh, *et al.*, A quantitative and qualitative comparative analysis of collagen fibers to determine the role of connective tissue stroma on biological behavior of

odontogenic cysts: A histochemical study, *Natl. J. Maxillofac. Surg.*, 2012, **3**(1), 15–20.
49 B. L. Trus and K. A. Piez, Compressed microfibril models of the native collagen fibril, *Nature*, 1980, **286**(5770), 300–301.
50 L. N. Niu, *et al.*, Collagen intrafibrillar mineralization as a result of the balance between osmotic equilibrium and electroneutrality, *Nat. Mater.*, 2017, **16**(3), 370–378.
51 L. B. Gower and D. J. Odom, Deposition of calcium carbonate films by a polymer-induced liquid-precursor (PILP) process, *J. Cryst. Grow.*, 2000, **210**(4), 719–734.
52 S. C. Liou, S. Y. Chen and D. M. Liu, Manipulation of nanoneedle and nanosphere apatite/poly(acrylic acid) nanocomposites, *J. Biomed. Mater. Res., Part B*, 2005, **73**(1), 117–122.
53 K. He, *et al.*, Revealing nanoscale mineralization pathways of hydroxyapatite using in situ liquid cell transmission electron microscopy, *Sci. Adv.*, 2020, **6**(47), eaaz7524.
54 B. P. Pichon, *et al.*, A quasi-time-resolved CryoTEM study of the nucleation of CaCO3 under Langmuir monolayers, *J. Am. Chem. Soc.*, 2008, **130**(12), 4034–4040.
55 E. M. Pouget, *et al.*, The initial stages of template-controlled CaCO3 formation revealed by cryo-TEM, *Science*, 2009, **323**(5920), 1455–1458.
56 S. E. Wolf, *et al.*, Early homogenous amorphous precursor stages of calcium carbonate and subsequent crystal growth in levitated droplets, *J. Am. Chem. Soc.*, 2008, **130**(37), 12342–12347.
57 E. DiMasi, *et al.*, Laser Light Scattering Observations of Liquid–Liquid Phase Separation in a Polymer-Induced Liquid-Precursor (PILP) Mineralization Process, *MRS Online Proc. Libr.*, 2005, **873**, K10-6.
58 D. Gebauer, A. Völkel and H. Cölfen, Stable prenucleation calcium carbonate clusters, *Science*, 2008, **322**(5909), 1819–1822.
59 R. Demichelis, *et al.*, Stable prenucleation mineral clusters are liquid-like ionic polymers, *Nat. Commun.*, 2011, **2**, 590.
60 D. Gebauer, *et al.*, Pre-nucleation clusters as solute precursors in crystallisation, *Chem. Soc. Rev.*, 2014, **43**(7), 2348–2371.
61 J. W. Cahn and J. E. Hilliard, Free Energy of a Nonuniform System. III. Nucleation in a Two-Component Incompressible Fluid, *J. Chem. Phys.*, 1959, **31**, 688–699.
62 H. Cölfen and S. Mann, Higher-order organization by mesoscale self-assembly and transformation of hybrid nanostructures, *Angew. Chem., Int. Ed.*, 2003, **42**(21), 2350–2365.
63 E. Ruckenstein, G. O. Berim and G. Narsimhan, A novel approach to the theory of homogeneous and heterogeneous nucleation, *Adv. Colloid Interface Sci.*, 2015, **215**, 13–27.
64 P. R. ten Wolde and D. Frenkel, Enhancement of protein crystal nucleation by critical density fluctuations, *Science*, 1997, **277**(5334), 1975–1978.
65 J. J. De Yoreo, *et al.*, CRYSTAL GROWTH, Crystallization by particle attachment in synthetic, biogenic, and geologic environments, *Science*, 2015, **349**(6247), aaa6760.
66 I. E. Chesnick, *et al.*, Magnetic resonance microscopy of collagen mineralization, *Biophys. J.*, 2008, **95**(4), 2017–2026.
67 E. Osorio, *et al.*, Ethanol Wet-bonding Technique Sensitivity Assessed by AFM, *J. Dent. Res.*, 2010, **89**, 1264–1269.
68 M. Takahashi, *et al.*, The importance of size-exclusion characteristics of type I collagen in bonding to dentin matrices, *Acta Biomater.*, 2013, **9**(12), 9522–9528.
69 L. Dai, *et al.*, Inorganic-Organic Nanocomposite Assembly Using Collagen as Template and Sodium Tripolyphosphate as A Biomimetic Analog of Matrix Phosphoprotein, *Cryst. Growth Des.*, 2011, **11**(8), 3504–3511.
70 F. L. Barroso da Silva, M. Boström and C. Persson, Effect of charge regulation and ion-dipole interactions on the selectivity of protein-nanoparticle binding, *Langmuir*, 2014, **30**(14), 4078–4083.
71 M. J. Olszta, *et al.*, Nanofibrous Calcite Synthesized *via* a Solution-Precursor-Solid Mechanism, *Chem. Mater.*, 2004, **16**, 2355–2362.
72 M. J. Olszta, *et al.*, A new paradigm for biomineral formation: mineralization via an amorphous liquid-phase precursor, *Connect. Tissue Res.*, 2003, **44**(1), 326–334.
73 Y. Y. Kim, E. P. Douglas and L. B. Gower, Patterning inorganic (CaCO3) thin films *via* a polymer-induced liquid-precursor process, *Langmuir*, 2007, **23**(9), 4862–4870.
74 J. W. Smith, Molecular pattern in native collagen, *Nature*, 1968, **219**(5150), 157–158.
75 D. F. Holmes, H. K. Graham and K. E. Kadler, Collagen fibrils forming in developing tendon show an early and abrupt limitation in diameter at the growing tips, *J. Mol. Biol.*, 1998, **283**(5), 1049–1058.
76 D. F. Holmes, *et al.*, STEM/TEM studies of collagen fibril assembly, *Micron*, 2001, **32**(3), 273–285.
77 T. Tsuji, *et al.*, Direct transformation from amorphous to crystalline calcium phosphate facilitated by motif-programmed artificial proteins, *Proc. Natl. Acad. Sci. U. S. A.*, 2008, **105**(44), 16866–16870.
78 S. Gajjeraman, *et al.*, Matrix macromolecules in hard tissues control the nucleation and hierarchical assembly of hydroxyapatite, *J. Biol. Chem.*, 2007, **282**(2), 1193–1204.
79 N. Clemente, *et al.*, Osteopontin Bridging Innate and Adaptive Immunity in Autoimmune Diseases, *J. Immunol. Res.*, 2016, 7675437.
80 R. Xing, *et al.*, Colloidal Gold–Collagen Protein Core–Shell Nanoconjugate: One-Step Biomimetic Synthesis, Layer-by-Layer Assembled Film, and Controlled Cell Growth, *ACS Appl. Mater. Interfaces*, 2015, **7**(44), 24733–24740.